A magnetic data correction workflow for sparse, four dimensional data (MDCWS-4D)

Alan R.A. Aitken[1,1], Lara Nigro Ramos[1,1], Jason L Roberts[2,2], Jamin Stevens Greenbaum[3,3], Lenneke M Jong[2,2], Duncan Alexander Young[3,3], and Donald D Blankenship[3,3]

[1]University of Western Australia
[2]Australian Antarctic Division
[3]University of Texas at Austin

November 30, 2022

Abstract

High-quality aeromagnetic data are important in guiding new knowledge of the solid earth in frontier regions, such as Antarctica, where these data are often among the first data collected. The difficulties of data collection in remote regions often lead to less than ideal data collection, leading to data that are sparse and four-dimensional in nature. Standard aeromagnetic data collection procedures are optimised for the (nearly) 2D data that are collected in industry-standard surveys. In this work we define and apply a robust magnetic data correction approach that is optimised to these four dimensional data. Data are corrected in three phases, first with operations on point data, correcting for spatio-temporal geomagnetic conditions, then operations on line data, adjusting for elevation differences along and between lines and finally a line-based levelling approach to bring lines into agreement while preserving data integrity. For a large-scale East Antarctic survey, the overall median cross-tie error reduction error reduction is 93%, reaching a final median error of 5 nT. Error reduction is are spread evenly between phase 1 and phase 3 levelling operations. Phase 2 does not reduce error directly but permits a stronger error reduction in phase 3. Residual errors are attributed to limitations in the ability to model 4D geomagnetic conditions and also some limitations of the inversion process used in phase 2. Data have improved utility for geological interpretation and modelling, in particular quantitative approaches, which are enabled with less bias and more confidence.

A magnetic data correction workflow for sparse, four dimensional data

Alan R.A. Aitken[1], Lara Nigro Ramos[1], Jason L. Roberts[2], Jamin S. Greenbaum[3], Lenneke M. Jong[2], Duncan A. Young[3], Donald D. Blankenship[3]

1 – The School of Earth Sciences, The University of Western Australia, Crawley, Western Australia 6009, Australia

2 – The Australian Antarctic Division, Kingston, Tasmania 7050, Asutralia

3 – The University of Texas Institute for Geophysics, J.J. Pickle Research Campus, Austin, Texas, USA

Corresponding author: Alan Aitken (alan.aitken@uwa.edu.au)

Key Points

- A new approach to correcting four dimensional aeromagnetic data is developed and tested with the large-scale ICECAP dataset from East Antarctica
- Substantial improvements in data quality and reliability are seen and error thresholds are well defined.
- These improvements in data quality support the investigation of subglacial geology and tectonics in magnetic data.

Abstract

High-quality aeromagnetic data are important in guiding new knowledge of the solid earth in frontier regions, such as Antarctica, where these data are often among the first data collected. The difficulties of data collection in remote regions often lead to less than ideal data collection, leading to data that are sparse and four-dimensional in nature. Standard aeromagnetic data collection procedures are optimised for the (nearly) 2D data that are collected in industry-standard surveys. In this work we define and apply a robust magnetic data correction approach that is optimised to these four dimensional data. Data are corrected in three phases, first with operations on point data, correcting for spatio-temporal geomagnetic conditions, then operations on line data, adjusting for elevation differences along and between lines and finally a line-based levelling approach to bring lines into agreement while preserving data integrity. For a large-scale East Antarctic survey, the overall median cross-tie error reduction error reduction is 93%, reaching a final median error of 5 nT. Error reduction is are spread evenly between phase 1 and phase 3 levelling operations. Phase 2 does not reduce error directly but permits a stronger error reduction in phase 3. Residual errors are attributed to limitations in the ability to model 4D geomagnetic conditions and also some limitations of the inversion process used in phase 2. Data have improved utility for geological interpretation and modelling, in particular quantitative approaches, which are enabled with less bias and more confidence.

Plain Language Summary

Observations of the Earth's magnetic field underpin our knowledge of geology and tectonics, and are often among the first data collected in frontier regions. This work focuses on the problems experienced in remote surveys, including observation periods extending over years, and flying heights that vary over kilometres. Conventional approaches are designed for more tightly constrained survey collection and can be inappropriate for these data. A new way to process airborne observations of magnetic field intensity is developed and tested. Applied to a dataset in East Antarctica, the data quality is substantially improved and the data better reveals the geology hidden beneath the ice of Antarctica.

Index Terms

0925, 0910, 0903

1 Introduction

Since the beginnings of plate tectonic theory, observations of the Earth's magnetic field have been essential to understanding the structure and evolution of both continents and oceans [*Behrendt and Wotorson*, 1970; *Vine and Matthews*, 1963]. Commonly, magnetic data is one of the first geophysical data sets collected, forming the basis for subsequent investigations of the solid earth with other techniques. Good quality data is essential for the robust interpretation of tectonic systems, including the identification of major tectonic structures, and the internal structuring of tectonic domains, the definition of sedimentary basins, and clear mapping of magnetic polarity reversals in the oceanic crust.

In many parts of the world, in particular in regions with resource exploration activity, magnetic data have been systematically collected in regular surveys [*Nabighian et al.*, 2005]. High Resolution Aeromagnetic (HRAM) Data is collected at low-flying heights, often < 100m, consistently draped over topography and with individual surveys occurring over a short time period. Lines are arranged in parallel arrays, with spacings often < 1 km. For these surveys, robust data processing workflows exist, being well suited to the survey design and goals typically resulting in a representative data-grid [*Nabighian et al.*, 2005]. Either the line data or the grid can then be interpreted and modelled to provide knowledge of the solid Earth.

In other parts of the world, for example in frontier regions, data like these are not widely available either due to a lack of surveying or due to data being proprietary, and the only data available are often from large-scale reconnaissance surveys. These regions are where we, in general, know least about the magnetic structure of the solid earth, and so there is a need to maximise the value of these surveys. Datasets in these regions are defined, overall, by more irregular line directions and spacings, very variable flying heights and terrain separations and by much longer time-frames of data collection.

One such region is Antarctica, where data-coverage has been accumulated over decades through many airborne and marine surveys [*Chiappini et al.*, 2002; *A. Golynsky et al.*, 2013; *Alexander Golynsky et al.*, 2006; *A V Golynsky et al.*, 2018; *Kim et al.*, 2007]. Given the lack of outcrop information in Antarctica, these data provide a crucial resource to the understanding of the continental interior, including important aspects such as defining the locations of major tectonic structures [*A. R. A. Aitken et al.*, 2014; *Ferraccioli et al.*, 2011; *Tinto et al.*, 2019], defining sedimentary basins [*A. R. A. Aitken et al.*, 2014; *Ferraccioli et al.*, 2009a; *Frederick et al.*, 2016; *Tinto et al.*, 2019] and mapping major magmatic suites [*Behrendt et al.*, 1996; *Ferraccioli et al.*, 2009b]. The knowledge gained from these surveys is often critical for understanding the tectonics of Gondwana and earlier supercontinents [*A. R. A. Aitken et al.*, 2016; *Jordan et al.*, 2017; *Ruppel et al.*, 2018], as well as understanding the conditions at the base of the Antarctic Ice Sheet, in particular geothermal heat flux [*Martos et al.*, 2018].

Many airborne geophysical data surveys in Antarctica have a sparse and sometimes irregular data distribution, with data collection at a variety of flying heights and over longer time periods than a typical exploration-focused survey, often across multiple field seasons, and sometimes with multiple aircraft and instrumentation suites. Antarctic survey grids, in most cases, have line-spacings of 5 km or more and may be considered sparse, in the sense that the line spacing is typically greater than the source-sensor separation, leading to aliasing in the survey data, at least in the across-line direction [*Reid*, 1980]. Additional complications include logistical considerations surrounding the cost and complexity of installing remote camps, which promotes the collection of data in long flights undertaken from the widely separated permanent research stations. As a consequence, the survey may occur well away from supporting infrastructure, notably geomagnetic base stations (Fig. 1). In addition, as flight-time increases, regular aligned grids with close spacings become logistically infeasible. The survey may also traverse changing geomagnetic conditions over these long distances and long flight times, with little opportunity to provide cross-validation. The magnetic-polar location is a particularly challenging environment, exacerbated by the inability often to schedule flights explicitly in quiet geomagnetic conditions [*Damaske*, 1989; *Saltus and Kucks*, 1995]. Finally, the need to combine multiple forms of data in one platform (often, surface mapping lidar, ice penetrating radar, gravity and magnetic data) leads to further compromises in flight-design and collection procedures. These data are not well-suited to conventional data processing approaches, and a different approach is necessary to generate representative data products, and to maximise benefit to interpretation.

In this paper a data correction workflow is developed and tested, seeking to tackle the specific challenges of sparse and four dimensional data. The aim is to reduce, as far as possible, physically predictable spatio-temporal influences on the data before more pragmatic data adjustment procedures are applied. In particular, with a sparse 4D survey, the assumed inter-line relationships that underpin intersection-based or neighbour-based levelling are not necessarily valid. Finally, we seek a workflow that has minimal human data-value decisions, that is largely automated and that can accommodate new data being added with minimal re-adjustment to existing data. This allows an update at the end of each campaign, or in the case of a compilation such as ADMAP, updating as new surveys are added to the database. We apply this approach to a major airborne magnetic dataset from Antarctica, ICECAP [*A. R. A. Aitken et al.*, 2014; *Blankenship et al.*, 2011, updated 2013], which typifies the problems listed above.

A particular consideration is to maximise the value of these data for subsurface geological interpretation and modelling to contribute knowledge of subglacial geology. Applications in Antarctica include constraining knowledge of past and current ice sheet states, and in particular to enable the mapping of sedimentary basins [*A. R. A. Aitken et al.*, 2014; *Ferraccioli et al.*, 2009a], sub-ice-shelf cavities and lakes [*Greenbaum et al.*, 2015; *Tinto et al.*, 2019], and the identification of potentially high heat flux areas [*Carson et al.*, 2014; *Martos et al.*, 2018].

2 ICECAP data

The ICECAP data used here span surveys conducted in two multi-year stages. The first stage (ICECAP-I) includes campaigns from the 2008-2009 season to the 2012-2013 season [*Blankenship et al.*, 2011, updated 2013], and were previously published in Aitken et al [2014] and included in the most recent ADMAP-2 compilation [*A V Golynsky et al.*, 2018]. The second stage (ICECAP-II) includes here the data from campaigns in the 2015-16 and 2016-2017 seasons [*Roberts et al.*, 2018]. These were not included in the most recent ADMAP-2 compilation [*A V Golynsky et al.*, 2018]. Earlier ICECAP-I data processing focused on deriving an interpretable image, and included conventional steps such as base-station correction, removal of the International Geomagnetic Reference Field (IGRF) and intersection-based levelling [*A. R. A. Aitken et al.*, 2014].

All data collection was undertaken from a Basler BT-67 aircraft, registered C-GJKB, owned and operated by Kenn Borek Air, Ltd. A Geometrics 823A Caesium Vapour magnetometer was mounted in a tail boom, while positioning is provided from central, tail and wingtip mounted GPS sensors. Surface elevation data and ice thickness data was generated from UTIG HiCARS and HiCARS-2 ice penetrating radar systems [*Blankenship et al.*, 2012, updated 2013a]. The surface elevation data was supplemented by Riegl laser-altimeter data [*Blankenship et al.*, 2012, updated 2013b]. Survey priorities were different in different seasons, with initially the focus on large-scale coverage through long radial lines, then subsequently a focus on coastal regions in more conventional grid patterns (Fig. 1). Throughout the program satellite-tracks were flown, also older traverse lines, as well as transit flights and line re-flights. In the data-sparse environment of Antarctica, all these ancillary flights are important to improve coverage.

3 Correction Workflow

The characteristics discussed above lead to a complex data-processing environment demanding, as a particular limitation beyond those of more typical data, the reconciliation of data from different years, different flight heights, different line orientations, at large distances from base stations, and with varying geomagnetic field conditions. Initial data for this study is the raw data with only basic field QC procedures applied [*Blankenship et al.*, 2011, updated 2013; *Roberts et al.*, 2018].

The new processing workflow presented here comprises three phases, each with increasing data-connection (Fig. 2): Phase 1 involves point-by-point operations on individual data points; phase 2 includes line-by-line operations on individual lines and phase 3 includes multi-line operations on inter-line relationships.

Throughout the workflow, several software packages were used, including Oasis Montaj® for database handling and basic data operations, python, POMME [*S. Maus et al.*, 2010] and escript [*Gross et al.*, 2015]. Only POMME and escript have specific properties, and each is open-source; there is no dependence on proprietary techniques. The new approaches used in this study are described in the supporting information.

3.1 Phase 1 – Point-by-point operations

These data-processing steps are derived taking into account the large spatial and temporal scale of the dataset covering large distances and multiple years. The large volume of data (203 000 line km) and a desire for consistency and repeatability demanded a semi-automated process with minimal human intervention. Several steps are included in phase 1 – basic QC and denoising, IGRF removal [*Thébault et al.*, 2015], correction of spatio-temporal field variations with POMME [*S. Maus et al.*, 2010], and correction of the residual time-varying field with regional base station data.

3.1.1 Methods

3.1.1.1 Data import, QC and de-noising

All data were imported from native ASCII text formats into databases, and data were checked for obviously erroneous values, NaNs, missing data, and other such problems. These were corrected if possible, or the data omitted from further steps if not feasible. Locally noisy data was accounted for using the fourth difference transform [*Hood et al.*, 1979] applied to the time-series data. In the fourth difference processing, data was excluded where a magnitude threshold (unscaled) of 20 was exceeded. A Dirac delta function of *x* nT provides a 4th difference magnitude of *6x*, while a Heaviside step function of *x* nT provides a 4th difference magnitude of *3x*. Correspondingly, the threshold applied will allow single-point “spikes” of up to 3.33 nT and single-interval “steps” of up to 6.67 nT.

Following thresholding, an automatic routine was used to correct for minor spikes in the data. The routine looks in the fourth difference transform for a sufficient closeness to the characteristic fourth difference pattern of *0x, +1x, -4x, +6x, -4x, +1x, 0x*, where *x* is the magnitude of the spike. The need for this correction was identified with a moving window, considering both the numerical defect from this pattern, defined as $|i_{n-2} + i_{n-1}/-4 + i_n/6 + i_{n+1}/-4 + i_{n+2}|$ and the symmetricity observed, defined as $(4 \times |(i_{n+1}-i_{n-1})/((i_{n+1}+i_{n-1})/2)| + |(i_{n+2}-i_{n-2})/((i_{n+2}+i_{n-2})/2)|)/5$. If both defect and symmetry were below a tolerance of 0.5, a correction was applied based on $i_n/6$.

A procedure was also run to identify steps based on their own characteristic signature in 4th difference transform, i.e. *0x,1x,-3x,3x,-1x,0x* where *x* is a step between stations 3 and 4. Using similar equations as for spikes, the size of the step was recorded, however the removal of steps is more nuanced than spikes, and so they were not corrected for here, but are flagged in the database for potential correction in more detailed future studies.

3.1.1.2 POMME Geomagnetic Modelling

POMME geomagnetic field models attempt to capture in a spherical harmonic model the Earth's geomagnetic field from the near surface to elevations of several thousand kilometres [*S. Maus et al.*, 2010]. In contrast to the IGRF/DGRF, which accounts for longer-term and long-wavelength magnetic field variations [*Thébault et al.*, 2015], POMME also includes the capacity to include the core, lithospheric magnetospheric and induced fields on much smaller length scales and shorter timescales [*S. Maus et al.*, 2010]. In this study we used the tenth iteration of the model, POMME-10. This model is based on satellite data from the CHAMP (July 2000 – September 2010), Oersted (January 2010 to June 2014), and Swarm (December 2013 to November 2015) satellite missions. For the IGRF we use the 2015 model (12th generation) [*Thébault et al.*, 2015].

The required components for POMME modelling were compiled for each data point. As a minimum, the latitude, longitude and elevation of the data point, and the time of data collection are required. For best results, several model components are needed to describe the state of the magnetosphere [*S. Maus et al.*, 2010]. Interplanetary Magnetic Field (IMF) data indices were obtained from OMNIWEB 1 minute data [*King and Papitashvili*, 2005], from which the y-component of magnetic flux (IMF-By) was extracted in Geocentric Solar Magnetospheric (GSM) coordinates, sampled 35 minutes prior to the data collection time. The merging electric field Em was also derived from OMNIWEB data, sampled 60 minutes prior to data collection time. The time lags accommodate delays in the geomagnetic effects of the solar wind relative to measurements at the bow shock [*Lühr and Maus*, 2010]. Hourly Est/Ist indices representing the external and internal components of the magnetospheric disturbance magnetic field [*Stefan Maus and Weidelt*, 2004] were obtained from the NOAA geomagnetism server, and sampled at the data collection time. Finally, to parameterise the effect of solar cycles on the ring current, and associated bias in the Est index the 10.7 centimeter solar flux [*Tapping*, 2013] was obtained from data collected at the Penticton Observatory, for which we use the 81-day central average of observed solar flux. This was sampled 20 months prior to the data collection date [*Lühr and Maus*, 2010]. Est/Ist and F10.7 coverage is complete over the survey period, but the OMNIWEB record has some periods lacking data. Gaps in the IMF-By and IMF-Em records of less than 2 hours were interpolated with a maximum entropy prediction algorithm. This approach maintains noise characteristics similar to the original data. Any remaining gaps were assigned default values of 0 for IMF-By and 0.5 for IMF-Em.

POMME is used here as an alternative to the IGRF, seeking to improve the representation of higher frequency components of the magnetic field in the data correction process. We visualise this using the long-term record from Scott Base from 2008/07/01 to 2013/06/30 (Fig. 3). Power spectral density for the full POMME correction for this record is similar to the IGRF at frequencies of 1 per 90 days or lower, but a substantial difference in power spectral density is seen for higher frequencies. POMME correction with default values for the magnetospheric components (i.e. IMF-By, IMF-Em, Est, Ist and F10.7) matches the IGRF more closely, although providing higher power to diurnal and sub-diurnal cycles. Despite being substantially higher powered than the IGRF, the power spectral density of POMME remains well below the observed signal (Fig. 3).

3.1.1.3 Multiple Base Station Correction

Following the POMME data correction process, an explicit base-station correction is applied to account for remaining temporal field variations at higher frequencies (Fig. 3). Conventional methods using a local base station directly are not appropriate here, and so we define a method for the use of multiple distant base stations, similar in concept to previous approaches [*Abraham et al.*, 2008]. The method accounts for several influences that are not accounted for in single station base-station procedures. First, it allows for multiple base stations to be included, for this study up to 6; second, the procedure smoothly and automatically transitions between base-stations as the flight-line traverses through space; third, the correction from each station is inverse distance weighted using a power law function, the order of which is able to be specified. Inverse distance weighting is applied relative to a variable scaling-factor dependent on the furthest included station. Observations distant from any station are minimally corrected, reducing the risk of over-correction, while those close to a station, or stations, will receive stronger corrections. The fourth consideration in the correction is the geomagnetic distance, given by the difference in inclination, and the procedure allows to exclude stations that are geomagnetically distant from the observation (e.g. MAW see Fig. 1). Finally, the procedure allows for the vertical damping of base station records, accounting for elevation differences. For this adjustment, a square plate model is used [*Telford et al.*, 1990], with a user-specified width – narrower plates provide stronger vertical damping.

Large corrections from distant stations are high risk, potentially causing over-correction, and so as a measure of the risk of over-correction from distant stations the "leverage" applied to the correction is calculated. Leverage is defined for each contributing base station as the magnitude of the station correction multiplied by the distance to that station relative to the length scale. Overall leverage is defined by the sum over all included stations. Leverage may be used to exclude high-risk corrections.

3.1.2 Base Station Data Application

Base station data are used here for two purposes. First we use the long-term station records for the period from 2008/07/01 to 2013/06/30, covering the ICECAP-I data collection, to test the point-by-point operations for effectiveness. These data also are used to correct the ICECAP-I data, while for ICECAP-II, we obtain the base station data only for the specific data collection periods.

Base station data were obtained from the International Real-time Magnetic Observatory Network (INTERMAGNET), with 1-minute sampling interval. The observatories available in the region were, Casey station (CSY), Dome C (DMC) Dumont d'Urville (DRV), Mawson (MAW), Scott Base (SBA) and Vostok (VOS). These six stations circumscribe the survey area (Fig. 1).

Of these stations, temporal data coverage is variable: DRV, MAW and SBA have complete long-term records with recovery respectively 99.5%, 99.7% and 99.6%. CSY is very nearly complete, excepting a period with no data for 33 days between 2012/10/09 and 2012/11/11, with 100% recovery during station "on" time. DMC covers the complete period, but with a prolonged period with no data (2009/06/30 to 2010/01/01), and lower recovery overall (96.9%). VOS data is available only from 2011/01/01 onwards, but has no data between 2012/12/31 and 2013/05/02. 99.6% recovery is achieved during station "on" time. Consequently CSY,DRV, MAW and SBA are consistently available during ICECAP-I surveying, but DMC and VOS had important drop outs in this time. For the ICECAP-II survey periods, recovery was essentially complete for all stations, with over 99.9% recovery rate during station "on" time. DMC was not operational from 2015/12/28 to 2016/01/07, however.

The 4th difference noise reduction measures reduced the bulk long-term noisiness of all stations, as indicated by the standard deviation (Fig. 4). Small reductions are seen at CSY,DMC,VOS and SBA, due to the loss of small amounts of noisy data, < 2%, and only minor corrections applied. DRV and MAW saw larger reductions due to the loss of substantial amounts of data, 12% data loss at MAW and 8% at DRV.

For all base station records the correction for POMME predictions sees a reduction in the variability of the signal, but with varying effectiveness (Fig. 4). Only small reductions in variability are seen for DRV of -1.7 nT (3.8%), for DMC of -2.3 nT (5.7%) and for VOS of -2.8 nT (6.5%). For DMC and VOS, this likely reflects their high altitude, whereas the effectiveness of POMME for DRV may be restricted by its position near the pole. Substantially greater variability reductions are seen for MAW of -7.8 nT (16.0%), for CSY of -12.7 nT (23.3%) and for SBA of -37.9 nT (45.1%).

Inter-base corrections are not part of the correction workflow for base station data (Fig 2) however we apply this here to the long term data records to establish the effectiveness of the method, and to optimise the parameters. For each base station record, we use low-pass filtered records from the other five stations to correct for residual geomagnetic field variations, especially at higher frequencies. Flight data are situated in between stations, and so this represents a "worst-case" scenario in terms of distances between stations. For the base-station correction, we tested the relative importance of the number of stations to be included, the order of the power law function and the cutoff period for the low pass filter. For all stations except MAW, testing suggests that the optimum variability reduction is made by including the nearest four stations, and by using an inverse distance weighting of order two (inverse distance squared). Filter periods of 30 minutes to 360 minutes were tested with the strongest result obtained for a period of 120 minutes. Shorter periods show over correction at CSY and DRV, while longer periods showed under-correction at VOS. These settings were adopted for the field data correction. Vertical damping was found to reduce, to a small extent, the variability at DMC and VOS, suggesting utility for high elevation data, but otherwise was ineffective, and was not used with field data. Corrections using just the nearest single station are markedly inferior at CSY, DRV and SBA, and more mildly inferior at DMC, VOS and MAW (Fig 4).

Relative to the POMME-corrected data, substantial reductions in variability are made for VOS of -12.7 nT (31.7%) and for DMC of -8.2 nT (21.6%). These stations are close together, and have similar geomagnetic characteristics. Smaller variability reductions are made for SBA of -4.8 nT (10.4%), DRV of -2.5 nT (5.8%) and CSY, of -0.1 nT (0.2%). Mawson is magnetically, and spatially, quite distant from the other stations, and the base-to base data correction fails for this station, with an increase in variability of 7.2 nT (17.6%). As a consequence of this poor result, for the field data correction, we set the maximum geomagnetic inclination difference at 10°; this value excludes all stations but VOS and MAW for data near MAW, while allowing data near DRV to receive corrections from CSY,DMC and SBA.

3.1.3 Field Data Application

As with base station data, flight-line data were checked for obviously erroneous values, location or time-tagging issues, NaNs, missing data, cultural effects and other such problems that were corrected if possible, with the data omitted from further steps if not feasible. The same fourth difference processing was applied to flight lines, first with a threshold of 20 to remove noisy data, and despiking, with steps identified but not removed automatically. Very few data were altered as a consequence of this process, and so all subsequent steps used the whole dataset, retaining the potential to mask the results according to these thresholds.

For field data, we must also allow for changes in spatial location as well as time. The POMME model resolves spatio-temporal variations in the magnetic field, including some of the lithospheric signal that we wish to retain. Therefore, to appropriately reduce the field data, we apply a correction that reduces our data to the IGRF-reduced data standard at a particular time, t_0, in this case the 1st of January 2010.

The first step is to remove the IGRF, which we calculate for each data point at time t_0, using the 12th generation model [*Thébault et al.*, 2015] for all data locations. This accounts only for the spatial variations in the geomagnetic field. Spatio-temporal variations from this standard are defined using POMME. We calculate the full POMME correction at the time of data collection, t_t, and also at the reference time, t_0. The difference between these provides an additional spatio-temporal geomagnetic correction for each data point, so removing temporal differences in the main field, magnetospheric and lithospheric components. The magnitude of these corrections may be substantial, up to 211.5 nT, with a mean of 41.6 nT, a median of 18.3 nT, and root-mean-square (RMS) of 62.7 nT for the ICECAP data.

Base-station corrections were applied to each field data-point using up to 4 base stations, with an inverse-distance-squared weighting, and without any vertical damping. Prior to filed-data correction the observatory records were corrected for POMME variations, demeaned and low-pass filtered with a minimum period of 120 minutes (Fig 2). The maximum geomagnetic distance permitted was an inclination difference of 10°, a little less than the difference between VOS and DRV (11.8°). As with the POMME correction, the magnitude of these corrections may be substantial, up to 277.0 nT, with a mean of 40.6 nT, a median of 29.7 nT, and RMS of 55.3 nT.

An evaluation of the merit of these data reductions can be made through analysis of residual cross-tie errors. In doing so it must be borne in mind that the survey is four-dimensional. Time differences associated with line intersections vary from several hours to several years, while elevation differences vary from a few metres to over 1 km. The majority of the intersections come from the denser surveys near the coast, therefore, intersection-based measures are not fully representative of the magnitude of error, nor its reduction, much of which occurs in the more remote areas with few line-intersections.

Cross-tie errors for the raw TMI data are up to 1325.1 nT, with an RMS error of 120.1 nT, a mean error of 90.9 nT and a median error of 71.4 nT (Fig. 5). As expected, the IGRF correction for spatial variation alone yields very little change to these values. On application of the spatio-temporal POMME correction, the maximum cross-tie error is unchanged, however the RMS, mean and median values are all reduced, to 101.7 nT, 75.1 nT and 56.7 nT respectively. In terms of RMS, this is a reduction of 15% from the raw data. Applying the base-station correction reduces cross-tie errors further, with the RMS reduced to 77.4 nT, the mean to 54.7 nT and the median to 38.2 nT. Overall, Phase-1 of data correction has reduced the cross-tie errors by approximately ~40%.

3.2 Phase 2 – Line-by-line operations - Elevation Adjustment

In phase 2, we seek to adjust for another major variable in the data, which is differential flying heights between lines. For ICECAP data, the data are collected at WGS84 ellipsoidal elevations varying from -43 m to 4199 m. Most of this is dictated by the presence of the ice sheet, but occasionally differences are due to operational requirements. Source-to-sensor separation distance is therefore highly varied, both between lines and also along lines, with as much as 5 km variation being seen on individual lines (e.g. Fig. 6). A common approach to mitigate this is to apply either field continuation or equivalent source methods [*Pilkington and Boulanger*, 2017]. Commonly used FFT-based techniques assume evenly-spaced data collection on a level 2D plane (or 1D line) and are not strictly valid for drape-to-level or drape-to-drape corrections, and their use can introduce substantial errors [*Phillips*, 1996].

An alternative to field continuation is to use an equivalent source method, through the generation of magnetic sources at the Earth surface to indirectly define the observed magnetic field, which can then be recomputed on another surface [*Pilkington and Boulanger*, 2017]. A variant of this is to pursue correction through inversion techniques, which allows for a more nuanced definition of the source, including sources that are extensive at depth, and have 3D geometries. Furthermore, modern inversion tools are optimised to deal with large datasets on HPC infrastructure and, while more computationally expensive, can provide stable results in a time-efficient manner. In this case we apply an inversion technique, applied using the open-source package escript [*Gross et al.*, 2015].

3.2.1 Method

escript solves the inversion problem using the finite element method. escript has several capabilities that lend itself to our purpose: First, the magnetic field is a continuous function, piecewise-defined, everywhere within the inversion domain. Consequently, with a single inversion run, multiple data-realisations can be derived, both above and below the original flight height, without any recomputation. For example, we may sample the calculated magnetic field at constant altitudes, or as “draped” surveys at various heights above the surface, or on any other geometry we may choose. In this case we analyse only the constant altitude product at 2 km elevation. A second advantage is that the inducing magnetic field may smoothly vary within the domain, and everywhere the correct intensity and field orientation can be used. This is essential for our long lines traversing, in some cases, highly variable geomagnetic conditions. Third, the method allows data lines to be reduced to a consistent data-derived standard of fit. Finally, the method is easily automated and while compute-intensive, can be run as a “set-and-forget” operation on modern HPC infrastructure.

The inversion approach operates on each line independently, and is automated. Several steps are undertaken: First the original flight lines, which may be curved, are cut into straight line-segments, permitting not more than a 45° turn over 10 km. Minimum line-segment length is 20 km. For input to inversion, data are reduced to a common sample frequency of 1 Hz (ca. 80-90m at the typical aircraft velocity). The data file provided to the inversion contains the following required information: longitude, latitude, along line distance, flight elevation, bed elevation, magnetic intensity, IGRF field intensity, inclination and declination. These data are derived from ICECAP data re-sampled at the magnetic data points. ICECAP radar data does not everywhere resolve bed topography, for example due to very deep ice, subglacial lakes and ice shelf cavities, and we fill data gaps with the BedMachine Antarctica model [*Morlighem*, 2019.]. escript has capacity for unstructured meshing, promising much reduced computational requirements, however for this work a regular rectilinear domain with cuboidal elements is used, due to easier automation of the domain building process.

First, a 3D inversion domain is built from the data file, in data-defined UVW coordinates, applying suitable padding to the ends, top, base and sides of the data extents. In our case we take the line-segment data file and define vertical (W) extents extending 2.5 km above the highest data elevation, and 1 km below the lowest bed elevation. In the along line direction (U), padding is added to each end of the domain of approximately 2 times the domain height, defined as above. The lateral (V) extent of the domain is 5 times the domain height. The element length (ΔU) is set everywhere to the average data-point interval in the data file (typically ca. 80-90 m), while element height (ΔW) is set to 50 m. In the lateral direction, just 7 elements are used, so the element size (ΔY) is much larger. Inversion therefore is essentially of a 2.5D nature [*Rasmussen and Pedersen*, 1979].

Second, the model is populated with the data. Magnetic data are located in the relevant elements, with the data-function defined at element-centroids on the central V-element only. All other functions are continuous functions defined on element nodes, extensive across all V elements. The solid Earth, within which and only within which we wish to permit susceptibility changes, is defined using a fuzzy set approach: First we define the set of elements that are not entirely above the local surface, to which “solid Earth” membership is assigned. Then, we define the set of elements that are not entirely below the surface, to which “not solid Earth” membership is applied. For elements that belong to both sets, we re-assign the solid Earth membership value according to the extent to which the element is occupied by the solid Earth. For example for an element extending from 0 to 50 m, if the surface elevation is 25 m, the solid Earth membership value would be 0.5. The susceptibility response of the model is scaled according to the solid Earth membership function (Fig. 6b). This implementation preserves the volume of the solid earth, but not the shape, so a suitable vertical separation of at least ΔU must be ensured to accommodate the meshing precision.

The model domain is also populated with the values of the inducing magnetic field, as described by the IGRF (here calculated at time t_0, and at the lowest bed-elevation in the input data). The inducing field is piecewise translated into UVW field components, accounting for the line orientation relative to true north (φ_U). φ_U is defined as the arctangent of the longitudinal distance over the latitudinal distance, ensuring quadrant is preserved (numpy.arctan2 function). The orientation is calculated over ten data points (~800-900m in this case). This avoids introducing sharp changes as a consequence of location errors or abrupt deviations from the overall line direction, but accommodates gradual turns and curvatures relative to the direction of true north.

To perform the inversion, the built in magnetic intensity inversion module of escript is called, to generate an approximate solution to the susceptibility required in the subsurface to explain the observed magnetic field intensity variations. We apply the inversion as a series of attempts to solve the problem, beginning with a highly regularized (i.e. smooth) solution, and progressively relaxing the regularization until the target RMS misfit is reached, or until a number of cycles have been completed without a suitable result. The trade–off parameter μ describes the relative importance of data fit to smoothness in the inversion cost function, with larger values emphasising data fit [*Gross et al.*, 2015].

Using the susceptibility solution derived, the associated magnetic field is sampled at the desired locations within the domain. In our case, we consider the field sampled at a constant elevation of 2000 m. This realisation gives an elevation adjusted version of the magnetic data, that is, they have been corrected for the varying flight elevation, but still contain topographic effects from variable bed topography. Draped realisations may be derived from the models, however, they are more prone to instability and error from the often highly variable subglacial topography, and the high degree of downward continuation that may be required.

The elevation adjustment may involve downward continuation of the survey which may also introduce errors into the data. In contrast to frequency-domain downward continuation, the result of the inversion approach is numerically stable for this adjustment. However, while the amplitudes of existing anomalies will be adjusted, downward-adjusted data will not gain short-wavelength components that may be present in genuine data collected at a lower elevation. Upward adjusted data will lose short wavelength components appropriately.

3.2.2 Application

963 line-segments were modelled using the Magnus supercomputer, a Cray XC40, located at the Pawsey Supercomputing Centre located in Perth Western Australia. The automated modelling procedure reads the data for an individual line from the overall database output in ASCII txt format, builds a domain and runs an inversion as described above.

In our application the target RMS misfit was 3 nT, and the maximum number of cycles permitted was 6, each cycle for up to 50 iterations or until convergence is reached. Convergence in escript occurs when the size of the model update from an iteration is below a certain tolerance factor of the overall model size [*Gross et al.*, 2015]; in this case the tolerance factor was $1e^{-4}$. Convergence does not imply a satisfactory result from the point of view of data misfit, therefore, multiple cycles may be needed. Between cycles, the model trade-off parameter, μ, was increased by an order of magnitude, beginning at $1e^{-1}$ up to a maximum of $1e^{4}$. At the conclusion of each cycle the model process was terminated, if RMS misfit was satisfactory, or if not, the results were passed into the next cycle.

Of the 963 line-segments, 893 satisfactorily reduced RMS misfit to less than 3 nT within 6 cycles. All but 13 lines had residual RMS misfits of less than 10 nT and the worst residual misfit was 29.9 nT. The elevation adjustments made were substantial. Adjustment to a constant elevation of 2000 m involved magnitudes up to 1981.6 nT, with a mean of 22.4 nT, a median of 11.9 nT, and RMS of 41.3 nT. Despite the substantial changes in magnetic field, there was little direct impact on mistie-reduction (Fig. 5).

Individual jobs used between one and twelve 24-cpu compute nodes, running for periods up to several hours. As an example, ASB_JKB0a_GL0211a, a large line with 8900 data points, was completed on 5 nodes in 3 hrs and 42 minutes, consuming 445 cpu-hours to achieve a final RMS misfit of 0.89 nT after 4 cycles of iterations. A shorter line, TOT_JKB2n_Y15b, with 1272 data points, was completed on 1 node in 52 minutes, consuming 21 cpu-hours to achieve a final RMS misfit of 2.22 nT after 3 cycles of iterations. Model run-time varied with the number of data points, coupled with the complexity of the magnetic field and subglacial topography.

3.3 Phase 3 – Multi-line operations - Levelling

Following these corrections, the overall cross-tie errors have been reduced by ~40%. In the final phase, we apply a two-stage levelling process to account for residual errors following these corrections. Unlike an HRAM survey, line-intersections in this data are associated with large differences in time and elevation. Although these differences are adjusted for, we may consider levelling in this case as an attempt to bring independent data into mutual agreement, rather than a correction as such. Implicitly, preserving the data integrity along the line is more important than ensuring a low crossover error with other lines. Therefore we apply a conservative line-based approach, comprising first a base-level adjustment (DC shift), and second spline-based levelling. Levelling is applied to both the corrected TMI data and to the data adjusted to an elevation of 2000 m.

3.3.1 Method

The ICECAP data do not everywhere possess a clear hierarchy or ordering of the line sets. Although many of the sub-surveys are flown with distinct orthogonal line sets, these are not well aligned with each other, and furthermore they overlap and are intersected by regional lines of a variety of orientations. Therefore inevitable problems emerge with respect to structuring the levelling approach. Two fundamental choices exist, being network-adjustment methods focusing on loop-closures, or line-based levelling using smooth functions which we use here.

3.3.1.1 Median Line Levelling

In the first stage, we seek to apply only a base-level adjustment to each line. With the ICECAP data, which has no particular line hierarchy, we must first define the hierarchy of lines, to specify the order of correction. A customised technique is developed, using the median cross-tie error on each line as representative of the adjustment needed.

Line-segment intersections are defined by cycling through line-segment pairs, and for each linear line-segment, recording the points on the target line-segment that are within 50 m of a point on the reference line-segments. With the linear line-segments, multiple crossings are not possible, and so for each line-segment pair, we seek one value that defines the cross-tie error, recording for the target line the point location, FID and the value adjustment required to match the reference line.

Our approach to levelling these lines uses the median cross-tie error from the intersection points to define the optimal correction for each line-segment. It may be the case, due to oblique intersections or where lines are coincident, that more than one point is returned as an intersection for any given line-segment pair. In this case the mean cross-tie error of the intersection points is assigned to the mean XY location of the intersection points, and so only one value is given for each line-segment pair.

Adjustments are applied in an iterative fashion. In the algorithm, the line-segments are ordered in “worst-first” order, based on the median cross-tie error for each line-segment. The algorithm adjusts the worst line-segment, and updates all the cross-ties on applicable reference lines. The algorithm then adjusts the second worst line and so on until all lines have been adjusted. Several iterations of this cycle are repeated, testing for convergence to a given standard, defined by the reduction of the highest line-segment median to a given value. The final adjustments are applied line-by-line to the data.

3.3.1.2 Spline-based Levelling

Following the median based line-levelling, the data set is able to be addressed with spline-levelling techniques. In practice, the optimum levelling approach at this stage depends on the desired application and target region. For this study we apply a conservative spline-levelling approach that is appropriate for application to the entire dataset. For each line-segment, the residual cross-tie errors after median-based levelling are calculated. Tie-points based on more than 5 reference points are excluded to eliminate highly oblique intersections, and the remainder are halved so as to factor in the corresponding adjustment to the reference line. A tensioned spline is fitted through these points, and the second derivative of the spline is calculated. For each line we apply an iterative procedure to remove points associated with high curvature: Each iteration removes the highest and lowest curvature points, if they also exceed a specified threshold. This process avoids human decisions over line-segment hierarchy and data value, and avoids over-correction of the data, at the cost of a systematic under correction. Residual errors may be dealt with manually for specific areas.

3.3.2 Application

For both the corrected TMI data and the elevation adjusted data, median-based levelling was applied to the 963 line-segments, for which 9,488 line-segment pairs were identified. 58 line-segments did not possess any intersections and are excluded. The levelling algorithm was applied with a desired standard of 1 nT and a maximum number of cycles of 20. For both the corrected TMI and elevation-adjusted TMI, convergence was achieved to the data standard before 20 cycles were completed. Post-correction, a further 45 line-segments were excluded due to visible line-correlated effects, lack of suitable cross-ties or erroneous values. Excluded line-segments were not levelled using the intersection values, but were brought into agreement with the rest of the data by applying a base-level adjustment derived from the mis-match of the data to a low-resolution (20 km) regional grid of the retained lines, after levelling.

Median-based line levelling is a powerful component of the correction process, resulting in substantial changes to the data (see supporting information), and the expected reduction in the overall cross-tie error (Fig. 5). For the corrected TMI, the largest adjustment applied through median line levelling was 1300.4 nT, the mean 31.2 nT, the median 17.0 nT and the RMS 42.7 nT. For the elevation adjusted TMI, adjustments were similar being up to 1305.2 nT, with a mean of 34.7 nT, a median of 20.6 nT and an RMS of 57.2 nT. The difference in magnitude occurs due to the de-meaning process applied during the elevation adjustment. The inversion uses de-meaned data, after which the mean is returned to the data without back-adjustment. If the elevation adjustment is not zero-mean (Fig. 7), then a base-level error is introduced. The result is that, although cross-tie errors overall slightly increased with elevation adjustment, this is easily corrected for and the elevation adjusted data is substantially more internally consistent once base-level adjustments have been applied (Fig. 5).

For each data set, spline levelling was applied with a tension of 1 and a smoothness of 0.7, giving a smooth adjustment overall, with the second derivative not exceeding $2e^{-5}$ nTm^{-2}. Two ten-iteration cycles of the spline-levelling algorithm were applied, recomputing intersections in between. In the corrected TMI dataset, 17,889 ties were initially available, with the final levelling using 13,950. With the elevation adjusted data, 17,889 ties were available, of which 14,087 were used in the final levelling.

For the corrected TMI, the change to the data from the spline-levelling process was less than in all the previous steps, with a maximum adjustment of 203.9 nT, a mean of 11.4 nT, a median of 5.6 nT, and an RMS of 20.5 nT. The residual RMS cross-tie error is reduced to 41.5 nT, the mean to 19.0 nT and the median to 5.9 nT. For the elevation adjusted data, results are similar with a maximum adjustment of 155.7 nT, a mean of 11.4 nT, a median of 5.7 nT, and an RMS of 19.8 nT. The residual RMS cross-tie error is reduced to 29.1 nT, the mean to 14.0 nT and the median to 4.8 nT (Fig. 5).

4 Results

The data processing has generated the corrected TMI at original flight elevation, and an elevation-adjusted dataset at 2000m above the WGS84 ellipsoid (Fig. 8). The latter is the superior product and has brought out many of the higher amplitude features beneath thick ice in the inland region. Similarly, some coastal anomalies are relatively subdued.

The elevation adjusted data can more safely be used in mapping, and especially so for any quantitative work that is sensitive to the amplitudes of anomalies, which in previous regional products are inconsistently defined due to differences in flying height [*A. R. A. Aitken et al.*, 2014; *A V Golynsky et al.*, 2018]. For example, in figure 8 (inset) we see more clearly the sub-linear anomalies in the inland region (e.g. *a*), that are now of comparable amplitude to those near the coast (e.g. *b*), suggesting a similar origin. In the corrected TMI the amplitude of these anomalies is lower, leading to the potential for misinterpretation.

5 Discussion

5.1 Utility of the results

The final cross-tie errors in general exceed our target of 3 nT, but are within the error threshold of large regional data-grid compilations, when compared with long survey lines [*Milligan et al.*, 2009] and the dataset is adequately precise for most regional investigations. Further adjustment on the basis of line-intersections would of course reduce these errors, but we consider that, due to the incomplete data corrections applied in phase 1 and phase 2, the data remain 4D, and so it is not valuable to pursue an exact fit through levelling.

Given the diverse nature of the ICECAP dataset, additional levelling procedures may be fruitful for specific purposes, for example traditional tie-line/flight line levelling can be applied to the high resolution grid-pattern surveys near the coast; while closed-loop methods may be valuable for the moderate-density regions (e.g. inset, Fig. 8). Our data processing provides a regionally consistent starting point for more targeted investigations at smaller scales.

The data, in particular the elevation adjusted data, are consistently processed and have a sufficiently small error threshold to be suitable for careful inclusion in automated and quantitative interpretation methods. The data remain aliased in areas with sparse data (e.g. inset, Fig. 8), and this can only properly be rectified by the addition of data. Finally, in the data presented here we do not correct for the shape of the topographic surface, and so there may be residual effects. For example, in figure 8 (inset) the Denman Glacier trough can be seen as a magnetic low, and the Totten and Moscow University ice shelves also have magnetic lows. At least part of this magnetisation deficit may be due to the low topography, however, geological processes, such as faulting or basin formation, are also plausible causes for reduced magnetisation.

5.2 Value of the workflow

A crucial question is the value of this approach relative to its cost, in comparison to other approaches. For each phase we can define some guidelines as to when this approach is beneficial. We consider firstly, the reduction of error in the data, but also the capacity of the data to resolve the magnetic structure of the solid earth without bias.

5.2.1 Phase-1

Point-by-point operations, in general, operate quickly on the data and are quite easily applied, so are relatively low cost. The need to collate and reformat data from widespread sources, including multiple base stations, and the magnetospheric components required for POMME is straightforward but relatively time-consuming. There is also some overhead with the input and output of data to external operations, such as POMME, in comparison to those that are integral to the data processing package, such as the IGRF, although this is offset by the large degree of automation possible. The POMME modelling itself is quite rapid, but may take some time for larger datasets. For example, in our implementation for the 2016/2017 dataset, run in serial on a Linux Workstation, total computation time was 40 minutes for ~266,000 datapoints (17,883 line km at 1 Hz sampling).

While it is essential to account for the secular magnetic field variation in a multi-year survey, we may consider if the more complex POMME model provides a substantially more accurate correction than the IGRF calculation. For the long-term base station records, comparison with the daily IGRF correction shows that variability after POMME correction is reduced for all stations, with standard deviations 1.2 to 2.1 nT lower ~ 2-5% of overall error. Although the bulk reduction on base station signal variability is not marked in comparison to the IGRF correction (Fig. 4), the numerical difference between POMME and IGRF is however not negligible. The overall differences between the full POMME model and the IGRF model range from -57 nT to 256 nT, with a median magnitude of 38 nT, and with substantial variations seen over a range of timescales, from annual to diurnal. For periods shorter than 90 days, although POMME possesses much greater power spectral density than the IGRF, it remains well below the power spectral density of the observatory-based records (Fig. 3), however. 4D geomagnetic models such as POMME may become higher-powered, and higher resolution, and there is scope for this approach to be more beneficial in the future, especially for data in remote locations far from base stations.

For the base station correction, computation time is negligible, and the power spectral density is comparable to the data down to periods of a few hours (Fig. 3). The multiple base station correction, applied between bases over a long-term cycle with four bases and an inverse distance squared scaling, is effective in the main, reducing the residual variability in the long-term base station records, except at MAW. In comparison, running the same correction with values from only the nearest base station yielded inferior results, with residual variability between 0.3 nT and 6 nT less in the multi-base correction (1% to 14%). The value of the multi-base correction is variable, with strong improvements for CSY, SBA and DRV, but weaker improvements for DMC, MAW and VOS where the correction is highly dominated by a single station. With field data, located between the base stations, the multiple-base-station correction process has a strong effect, reducing the cross-tie errors substantially, by ~ 20% relative to the POMME corrected data.

Overall, the actions performed in phase-1 reduce variability in the long-term base station records, with the largest proportional effect at SBA (reduced by 51%) and the weakest at DRV (17%). Reduction in the cross-tie errors of the flight data is also substantial, with the mean reduced by 40%, the median by 46% and the RMS by 36%. Substantial changes are made to the data, of the order of tens to hundreds of nT. Our testing suggests that the level of error reduction is in all cases greater than IGRF and single base station corrections, but perhaps not markedly so.

5.2.2 Phase-2

Phase-2 includes the geophysical inversion, which is used here to adjust the data to a constant elevation, although other transforms are possible within the inversion algorithm including the calculation of draped surveys, reduction to the pole and pseudogravity calculations. The data is implicitly smoothed, due to the smoothness requirements of the inversion. Fourier-domain filtering is commonly used to perform this continuation task, however alternatives such as equivalent point source methods may also be used more effectively [*Pilkington and Boulanger*, 2017].

The inversion process is free from theoretical assumptions inherent to the frequency domain approach, most notably the assumption that the potential field is evenly sampled on a plane (or line in 2D), rather than a complexly shaped surface, however it is substantially more complex and time-consuming than simple filtering. The inversion method is also superior to equivalent source methods in that the recovered susceptibility distribution is smooth, has a depth extent and so can accommodate dip, and involves off-profile magnetisation, albeit in a limited way. A stable mode of downward continuation is enabled, although this will not generate new short-wavelength information, except in the case of magnetisation of rough topography.

Our results show that the elevation adjustment generates notable improvement to the magnetic data, with substantially stronger and more consistent definition of the anomalies beneath the thick ice of interior Antarctica. In addition, while a direct reduction in cross-tie error was not seen, the elevation adjusted data was superior to unadjusted data after levelling (Fig 5). Compared to the corrected TMI, cross-tie errors in the elevation adjusted product were less by 12.4 nT for the RMS (30%), 5.0 nT for the mean (26%), and 1.1 nT for the median (19%).

5.2.3 Phase-3

Despite the preceding adjustments, the data retain 4D characteristics, and the applied levelling procedure is intended to be conservative, preserving the integrity of the individual lines, but accounting for inconsistencies as identified by cross-tie errors. In terms of the impact on cross-tie errors, the median-based line adjustment is substantial, accounting for ~ 30-35 % of the overall cross-tie error reduction. While applying a base-level adjustment is a purely numerical adjustment, it is a commonly accepted part of any data integration exercise, whether with grids or line data [*Minty et al.*, 2003]. The cost of application is low, as the levelling algorithm runs in seconds. The main advantage of the approach over typical approaches is that there is no requirement for a predefined line order or hierarchy, nor the need for an operator to make decisions about which lines need adjustment. While the median is a conservative choice, avoiding over-correction, it is in some cases biased by an uneven distribution of intersections.

Spline interpolation, although a very common and robust interpolation procedure, has no physical basis as a correction to magnetic data. Because it makes changes to the relative intensity of anomalies along each line, the spline levelling should be applied only once cross-tie errors are minimised. In our case the spline levelling is the smallest magnitude correction, in terms of nT, with a mean magnitude of ~16-25 nT and a median magnitude of ~6 nT.

The final RMS cross-tie error following phase 3 is 41.5 nT for the corrected TMI and 29.1 for the elevation adjusted data set; the means are 20.0 nT and 14.0 respectively, and the medians are 5.9 nT and 4.8 nT.

5.3 Residual Errors

Following this data correction workflow, the magnitude of error reduction, as defined by cross-tie errors is substantial. For the corrected TMI data, RMS error is reduced by 65%, with 79% reduction of the mean error, and 92% reduction of the median error. For the elevation-adjusted data, greater reductions are seen, by 76% (RMS), 85% (mean) and 93% (median), indicating the effect of the elevation adjustment. Despite these reductions, absolute values of cross-tie errors remain above our target precision of 3 nT. Residual errors are concentrated on several problematic lines, with residual cross-tie errors also concentrated near the peaks or troughs of high amplitude anomalies, or at regions of high gradient (Fig. 8). Further levelling may reconcile these errors, but the value of this process may be limited, as the data retains residual 4D characteristics. For a greater reduction to residual error, we may look more closely at improving our earlier corrections to the data, which are systematically insufficient.

Phase 1 corrections are underpowered with respect to the signal they are intended to correct (Fig. 3). This situation may improve as geomagnetic models like POMME become higher-powered, in particular for shorter periods, due to the inclusion of more detailed magnetic information [*S. Maus et al.*, 2010]. The base station correction, which in this case relies on quite distant stations, often with incomplete records, is inadequate with respect to removing diurnal and sub-diurnal intensity variations (Fig 3). Besides having more closely spaced base-stations, which is infeasible, improvement of the base-station correction may need a better approach to resolving four-dimensional geomagnetic conditions from base station data.

Elevation differences are in principle accounted for by the inversion process, however, while anomaly amplitudes are corrected, short-wavelength signals are missing in cases where the elevation is adjusted downwards. Therefore, high-elevation lines, where they intersect low-elevation lines, are not fully compatible, especially if the signal is rough at low elevations (Fig. 8). The inversion process is also not uniformly precise and, where 3D anomalies are involved, the 2.5D model structure may misrepresent the source geometry. Non-orthogonal strike and the effects of remanent magnetisation are not fully accounted for.

6 Conclusions

Our workflow to process data seeks to correct for several systemic errors in magnetic data correction that especially may have impact on sparse, four-dimensional surveys conducted across multiple years in remote environments. The workflow includes three phases considering data as individual points, lines and then sets of lines. With long-term base-station data we show that point-by-point corrections are effective in reducing the variability of the signal by 25 to 50 %, with a similar effect on reducing cross-tie errors at line intersections. These corrections are superior to a more simple workflow, although the numerical error-reduction is not marked.

Phase 2 adjusts for differences in data-collection elevation, in this case adjusting all data to an elevation of 2000 m, similar to the mean flight elevation of 2215 m. This step is effective in increasing the relative amplitudes of anomalies in inland locations, where they are buried beneath thick ice. A direct effect on cross-tie errors was not seen, however, the elevation adjusted data saw much larger error-reductions in later levelling, indicating superior data consistency. Although computationally intensive, the inversion process is superior to more simple approaches in that anomalies can be reliably downward adjusted, with an inherently smooth and realistic model of subsurface magnetisation.

Phase 3 constitutes the line-based levelling of the data, for which a median-based base-level adjustment was highly effective in reducing cross-tie errors. Spline-levelling was less effective, but reduced further the relatively small residual errors in the data. Leveling used a rapid semi-automated approach, requiring little human intervention.

The final results of this workflow [*A.R.A. Aitken and Nigro Rodrigues Alves Ramos*, 2019], while still not of comparable precision to tightly constrained HRAM datasets, reduced the initial errors by between 76% to 93%, depending on metric. Confidence and interpretability is improved compared to previous ICECAP data processing [*A. R. A. Aitken et al.*, 2014]. In particular, through elevation adjustment, the data in inland regions is brought to a similar standard to the coastal regions and can be interpreted without the systemic bias of flight altitude. This includes the use in automated procedures, in particular those that depend on anomaly amplitudes, such as texture-mapping. The improved data allow for new analysis to undertake more comprehensive tectonic and geological research in the region.

7 Acknowledgements

This research was supported through the Australian Antarctic Science Program project grant 4460. ICECAP and ICECAP-II data collection was supported through the Australian Antarctic Science Program project grants 3103, 4077 and 4346. This work was supported by resources provided by the Pawsey Supercomputing Centre with funding from the Australian Government and the Government of Western Australia. The data presented in this work is available from the Australian Antarctic Data centre (http://dx.doi.org/doi:10.26179/5e015bb8dce7f). Reviewers Fausto Ferraccioli and Tom Jordan provided valuable comments.

8 References

Abraham, J., et al. (2008), Aeromagnetic Survey in Afghanistan: A Website for Distribution of Data, *United States Geological Survey Open-file Report 2007-1247*.

Aitken, A. R. A., P. G. Betts, D. A. Young, D. D. Blankenship, J. L. Roberts, and M. J. Siegert (2016), The Australo-Antarctic Columbia to Gondwana transition, *Gondwana Research*, *29*(0), 136-152, doi:http://dx.doi.org/10.1016/j.gr.2014.10.019.

Aitken, A. R. A., and L. Nigro Rodrigues Alves Ramos (2019), Reprocessed Magnetic Data from ICECAP-I and ICECAP-II, 2008/2009 to 2016/2017, Ver. 1, edited, Australian Antarctic Data Centre, doi:10.26179/5e015bb8dce7f.

Aitken, A. R. A., D. A. Young, F. Ferraccioli, P. G. Betts, J. S. Greenbaum, T. G. Richter, J. L. Roberts, D. D. Blankenship, and M. J. Siegert (2014), The subglacial geology of Wilkes Land, East Antarctica, *Geophysical Research Letters*, 2014GL059405, doi:10.1002/2014GL059405.

Behrendt, J. C., R. Saltus, D. Damaske, A. McCafferty, C. A. Finn, D. Blankenship, and R. E. Bell (1996), Patterns of late Cenozoic volcanic and tectonic activity in the West Antarctic rift system revealed by aeromagnetic surveys, *Tectonics*, *15*(3), 660-676.

Behrendt, J. C., and C. S. Wotorson (1970), Aeromagnetic and gravity investigations of the coastal area and continental shelf of Liberia, West Africa, and their relation to Continental Drift, *Bulletin of the Geological Society of America*, *81*(12), 3563-3574, doi:10.1130/0016-7606(1970)81[3563:AAGIOT]2.0.CO;2.

Blankenship, D. D., S. D. Kempf, and D. A. Young (2011, updated 2013), IceBridge Geometrics 823A Cesium Magnetometer L2 Geolocated Magnetic Anomalies, Version 1, edited, NASA National Snow and Ice Data Center Distributed Active Archive Center, Boulder, Colorado USA., doi:http://dx.doi.org/10.5067/TO7WLC72UMAQ.

Blankenship, D. D., S. D. Kempf, and D. A. Young (2012, updated 2013a), IceBridge HiCARS 2 L2 Geolocated Ice Thickness, Version 1, edited, NASA National Snow and Ice Data Center Distributed Active Archive Center., Boulder, Colorado USA., doi: http://dx.doi.org/10.5067/9EBR2T0VXUDG.

Blankenship, D. D., S. D. Kempf, D. A. Young, J. L. Roberts, T. D. Van Ommen, R. Forsberg, M. J. Siegert, S. J. Palmer, and J. A. Dowdeswell (2012, updated 2013b), IceBridge Riegl Laser Altimeter L2 Geolocated Surface Elevation Triplets, Version 1, edited, NASA National Snow and Ice Data Center

Distributed Active Archive Center. , Boulder, Colorado USA., doi:http://dx.doi.org/10.5067/JV9DENETK13E.

Carson, C. J., S. McLaren, J. L. Roberts, S. D. Boger, and D. D. Blankenship (2014), Hot rocks in a cold place: High sub-glacial heat flow in East Antarctica, *Journal of the Geological Society*, *171*(1), 9-12.

Chiappini, M., F. Ferraccioli, E. Bozzo, and D. Damaske (2002), Regional compilation and analysis of aeromagnetic anomalies for the Transantarctic Mountains–Ross Sea sector of the Antarctic, *Tectonophysics*, *347*(1), 121-137, doi:https://doi.org/10.1016/S0040-1951(01)00241-4.

Damaske, D. (1989), Geomagnetic activity and its implications for the aeromagnetic survey in North Victoria Land, in *Geologisches Jahrbuch E38*, edited, pp. 41–58, Bundesanstalt fur Geowissenschaften und Rohstoffe, Hannover.

Ferraccioli, F., E. Armadillo, T. Jordan, E. Bozzo, and H. Corr (2009a), Aeromagnetic exploration over the East Antarctic Ice Sheet: A new view of the Wilkes Subglacial Basin, *Tectonophysics*, *478*(1-2), 62-77.

Ferraccioli, F., E. Armadillo, A. Zunino, E. Bozzo, S. Rocchi, and P. Armienti (2009b), Magmatic and tectonic patterns over the Northern Victoria Land sector of the Transantarctic Mountains from new aeromagnetic imaging, *Tectonophysics*, *478*(1-2), 43-61.

Ferraccioli, F., C. A. Finn, T. A. Jordan, R. E. Bell, L. M. Anderson, and D. Damaske (2011), East Antarctic rifting triggers uplift of the Gamburtsev Mountains, *Nature*, *479*(7373), 388-392.

Frederick, B. C., D. A. Young, D. D. Blankenship, T. G. Richter, S. D. Kempf, F. Ferraccioli, and M. J. Siegert (2016), Distribution of subglacial sediments across the Wilkes Subglacial Basin, East Antarctica, *Journal of Geophysical Research F: Earth Surface*, *121*(4), 790-813, doi:10.1002/2015jf003760.

Golynsky, A., et al. (2013), Air and shipborne magnetic surveys of the Antarctic into the 21st century, *Tectonophysics*, *585*, 3-12, doi:10.1016/j.tecto.2012.02.017.

Golynsky, A., et al. (2006), ADMAP — A Digital Magnetic Anomaly Map of the Antarctic, in *Antarctica: Contributions to Global Earth Sciences*, edited by D. K. Fütterer, D. Damaske, G. Kleinschmidt, H. Miller and F. Tessensohn, pp. 109-116, Springer Berlin Heidelberg, Berlin, Heidelberg, doi:10.1007/3-540-32934-X_12.

Golynsky, A. V., et al. (2018), New Magnetic Anomaly Map of the Antarctic, *Geophysical Research Letters*, *45*(13), 6437-6449, doi:10.1029/2018gl078153.

Greenbaum, J. S., et al. (2015), Ocean access to a cavity beneath Totten Glacier in East Antarctica, *Nature Geoscience*, *8*(4), 294-298, doi:10.1038/ngeo2388.

Gross, L., C. Altinay, and S. Shaw (2015), Inversion of potential field data using the finite element method on parallel computers, *Computers & Geosciences*, *84*(Supplement C), 61-71, doi:https://doi.org/10.1016/j.cageo.2015.08.011.

Hood, P. J., M. T. Holroyd, and P. H. McGrath (1979), Magnetic methods applied to base metal exploration, in *Geophysics and Geochemistry in the Search for Metallic Ores*, edited by P. J. Hood, pp. 77-104, Geological Survey of Canada, Economic Geology Report 31.

Jordan, T. A., F. Ferraccioli, and P. T. Leat (2017), New geophysical compilations link crustal block motion to Jurassic extension and strike-slip faulting in the Weddell Sea Rift System of West Antarctica, *Gondwana Research*, *42*, 29-48, doi:10.1016/j.gr.2016.09.009.

Kim, H. R., R. R. B. von Frese, P. T. Taylor, A. V. Golynsky, L. R. Gaya-Piqué, and F. Ferraccioli (2007), Improved magnetic anomalies of the Antarctic lithosphere from satellite and near-surface data, *Geophysical Journal International*, *171*(1), 119-126, doi:10.1111/j.1365-246X.2007.03516.x.

King, J. H., and N. E. Papitashvili (2005), Solar wind spatial scales in and comparisons of hourly Wind and ACE plasma and magnetic field data, *Journal of Geophysical Research: Space Physics*, *110*(A2), doi:10.1029/2004ja010649.

Lühr, H., and S. Maus (2010), Solar cycle dependence of quiet-time magnetospheric currents and a model of their near-Earth magnetic fields, *Earth, Planets and Space*, *62*(10), 14, doi:10.5047/eps.2010.07.012.

Martos, Y. M., M. Catalan, T. A. Jordan, A. Golynsky, D. Golynsky, G. Eagles, and D. G. Vaughan (2018), Heat flux distribution of Antarctica unveiled.

Maus, S., C. Manoj, J. Rauberg, I. Michaelis, and H. Lühr (2010), NOAA/NGDC candidate models for the 11th generation International Geomagnetic Reference Field and the concurrent release of the 6th generation Pomme magnetic model, *Earth, Planets and Space*, *62*(10), 729-735.

Maus, S., and P. Weidelt (2004), Separating the magnetospheric disturbance magnetic field into external and transient internal contributions using a 1D conductivity model of the Earth, *Geophysical Research Letters*, *31*(12), doi:10.1029/2004gl020232.

Milligan, P., B. Minty, M. Richardson, and R. Franklin (2009), The Australia-wide airborne geophysical survey - accurate continental magnetic coverage, *ASEG Extended Abstracts*, *2009*(1), 1-9, doi:https://doi.org/10.1071/ASEG2009AB075.

Minty, B. R. S., P. R. Milligan, A. P. J. Luyendyk, and T. Mackey (2003), Merging airborne magnetic surveys into continental-scale compilations, *Geophysics*, *68*(3), 988-995.

Morlighem, M. (2019.), MEaSUREs BedMachine Antarctica, Version 1. Boulder, Colorado USA. NASA National Snow and Ice Data Center Distributed Active Archive Center., edited, doi:https://doi.org/10.5067/C2GFER6PTOS4. [Date Accessed].

Nabighian, M. N., V. J. S. Grauch, R. O. Hansen, T. R. LaFehr, Y. Li, J. W. Peirce, J. D. Phillips, and M. E. Ruder (2005), The historical development of the magnetic method in exploration, *Geophysics*, *70*(6), 33-61.

P. Welch (1967), The use of fast Fourier transform for the estimation of power spectra: A method based on time averaging over short, modified periodograms *in IEEE Transactions on Audio and Electroacoustics*, *15*(2), 70-73.

Phillips, J. D. (1996), Potential-field continuation: Past practice vs. Modern methods, paper presented at 1996 SEG Annual Meeting.

Pilkington, M., and O. Boulanger (2017), Potential field continuation between arbitrary surfaces — Comparing methods, *GEOPHYSICS*, *82*(3), J9-J25, doi:10.1190/geo2016-0210.1.

Rasmussen, R., and L. B. Pedersen (1979), End corrections in potential field modeling, *Geophysical Prospecting*, *27*(4), 749-760.

Reid, A. B. (1980), Aeromagnetic survey design, *Geophysics*, *45*(5), 973-976.

Roberts, J. L., D. D. Blankenship, J. S. Greenbaum, L. H. Beem, S. D. Kempf, D. A. Young, T. D. Richter, T. G. Van Ommen, and E. Le Meur (2018), EAGLE/ICECAP II GEOPHYSICAL OBSERVATIONS (SURFACE AND BED ELEVATION, ICE THICKNESS, GRAVITY DISTURBANCE AND MAGNETIC ANOMALIES), Ver, 1, edited, Australian Antarctic Data Centre, doi:http://dx.doi.org/doi:10.26179/5bcfffdabcf92.

Ruppel, A., J. Jacobs, G. Eagles, A. Läufer, and W. Jokat (2018), New geophysical data from a key region in East Antarctica: Estimates for the spatial extent of the Tonian Oceanic Arc Super Terrane (TOAST), *Gondwana Research*, *59*, 97-107, doi:https://doi.org/10.1016/j.gr.2018.02.019.

Saltus, R. W., and R. P. Kucks (1995), Geomagnetic Activity and its Implications for the 1991–1992 Casertz Aeromagnetic Survey in Antarctica, in *Contributions to Antarctic Research IV*, edited, pp. 9-17, doi:10.1002/9781118668207.ch2.

Tapping, K. F. (2013), The 10.7 cm solar radio flux (F10.7), *Space Weather*, *11*(7), 394-406, doi:10.1002/swe.20064.

Telford, W. M., L. P. Geldart, and R. E. Sheriff (1990), *Applied Geophysics Second Edition*, 770 pp., Cambridge University Press.

Thébault, E., et al. (2015), International Geomagnetic Reference Field: the 12th generation, *Earth, Planets and Space*, *67*(1), 79, doi:10.1186/s40623-015-0228-9.

Tinto, K. J., et al. (2019), Ross Ice Shelf response to climate driven by the tectonic imprint on seafloor bathymetry, *Nature Geoscience*, *12*(6), 441-449, doi:10.1038/s41561-019-0370-2.

Vine, F. J., and D. H. Matthews (1963), Magnetic anomalies over oceanic ridges, *Nature*, *199*(4897), 947-949.

9 Figure Captions

Figure 1: ICECAP-I and ICECAP-II Data distribution by season. INTERMAGNET magnetic observatories are indicated in green with IAGA codes and observatory names: CSY – Casey Station, DMC – Dome C, DRV – Dumont d'Urville, MAW – Mawson, SBA – Scott Base, VOS – Vostok. Geomagnetic inclination contours are in red. The ice-sheet and ice-shelf surface is from BedMachine Antarctica [*Morlighem*, 2019.].

Figure 2: MDCWS-4D processing workflow. The workflow is divided into 3 main phases, each with greater data connectivity.

Figure 3: Power Spectral Densities (PSDs) for the Scott Base observatory record (SBA) from 2008/07/01 to 2013/06/30, showing PSDs for the observed magnetic field intensity, the IGRF, the POMME model with the magnetospheric components (full) and with default values for these (main). Also shown is the base-to-base correction calculated for SBA from the other base stations. PSDs are calculated with Welch's method [*P. Welch*, 1967] using 1-minute data with a window size of 90 days. IGRF data are calculated daily, so are not shown for frequencies above 0.5 per day.

Figure 4: Signal variability reductions for long-term observatory records with the applied point-by-point corrections. Variability is expressed as the standard deviation of the entire long-term record, from 2008/07/01 to 2013/06/30, in nT. Base-to-Base and IGRF corrections are not part of the base-station processing workflow, but are shown to indicate the effectiveness of these.

Figure 5: Correction magnitudes (columns) and associated cross-tie error reductions (lines) for field data. Cross-tie errors at line intersections are interpreted as indicating residual error.

Figure 6: Inversion setup for a single line. GL0211a is a coast-perpendicular line extending from Law Dome inland towards the Aurora Subglacial Basin (location in Fig. 1). A) shows the whole line with data location and subsurface masking. The surface of the ice sheet (grey line) is shown here but is not part of the model. Source-sensor separation varies between ~ 1. 5 km to almost 5 km. B) An inset showing at fine scale the effective susceptibility scaling (k-scaling) of the model, with the mesh superimposed. The region between the black and white lines delineates the transitional cells with variable k-scaling. K-scaling is uniformly 1 beneath, and 0 above. Elements in this case are 50m high and 82 m wide.

Figure 7: Data for ASB_JKB0a_GL0211a showing A) the corrected TMI data and the elevation adjusted TMI at an elevation of 2 km. B) the elevation adjustment made to the data. C) The susceptibility model, the elevations sampled and also the ice sheet surface and bed elevation, with inset as in Fig 6.

Figure 8: Fully processed data, in A the corrected TMI; in B the elevation adjusted data at 2000m elevation. In each case the left panel shows the overall dataset, while the insets on the right show a zoomed in view of the western Wilkes Land (top) and the associated residual cross-tie errors (bottom). All images use the same colour-scale. For other steps in the workflow, please refer to the supporting information.

Figure 1.

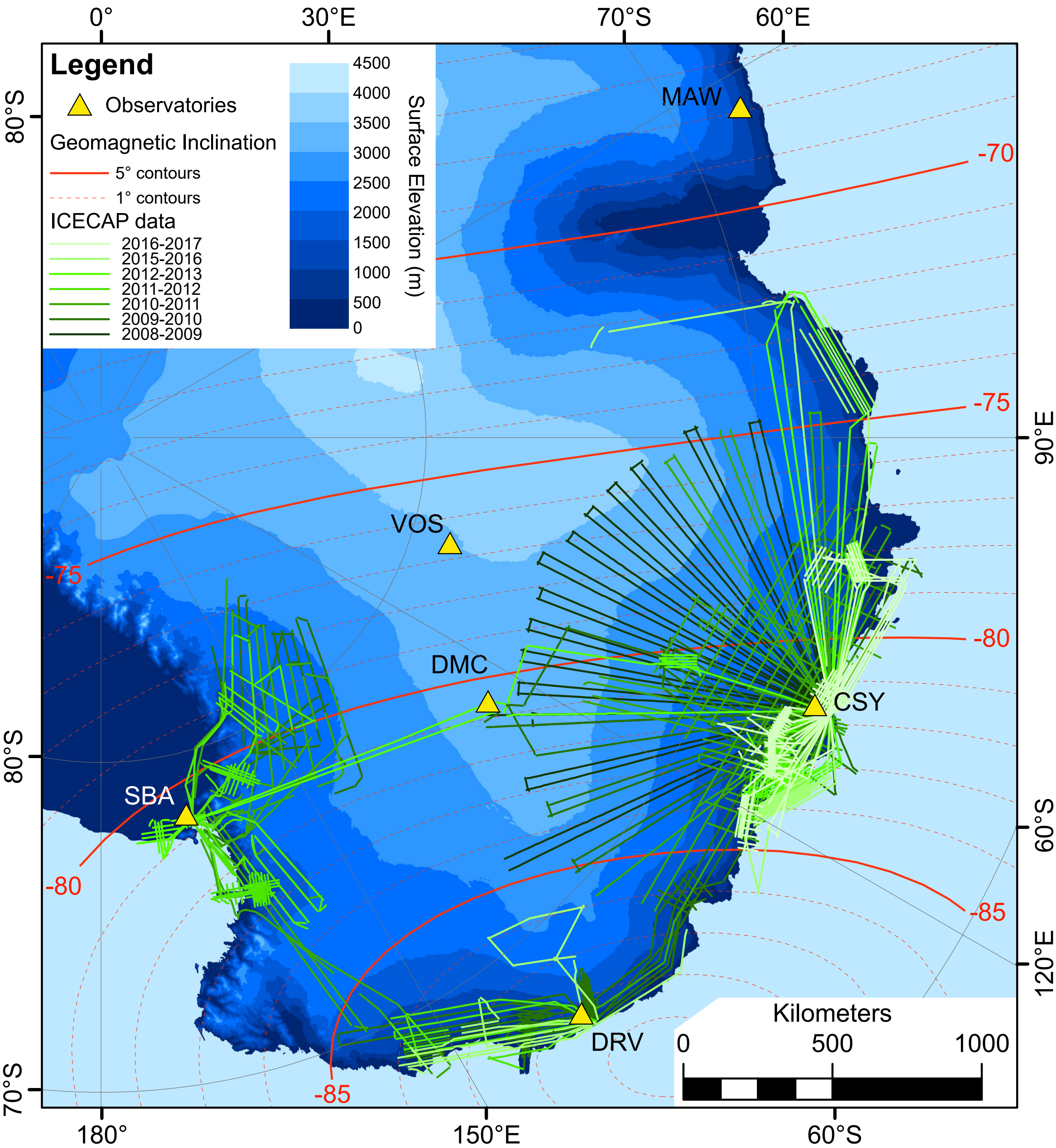
Legend
Observatories
Geomagnetic Inclination
5° contours
1° contours
ICECAP data
2016-2017
2015-2016
2012-2013
2011-2012
2010-2011
2009-2010
2008-2009
4500
4000
3500
3000
2500
2000
1500
1000
500
0
Surface Elevation (m)
0°
30°E
70°S
60°E
80°S
90°E
60°S
120°E
70°S
180°
150°E
60°S
MAW
VOS
DMC
CSY
SBA
DRV
-70
-75
-75
-80
-80
-85
-85
Kilometers
0
500
1000

Figure 2.

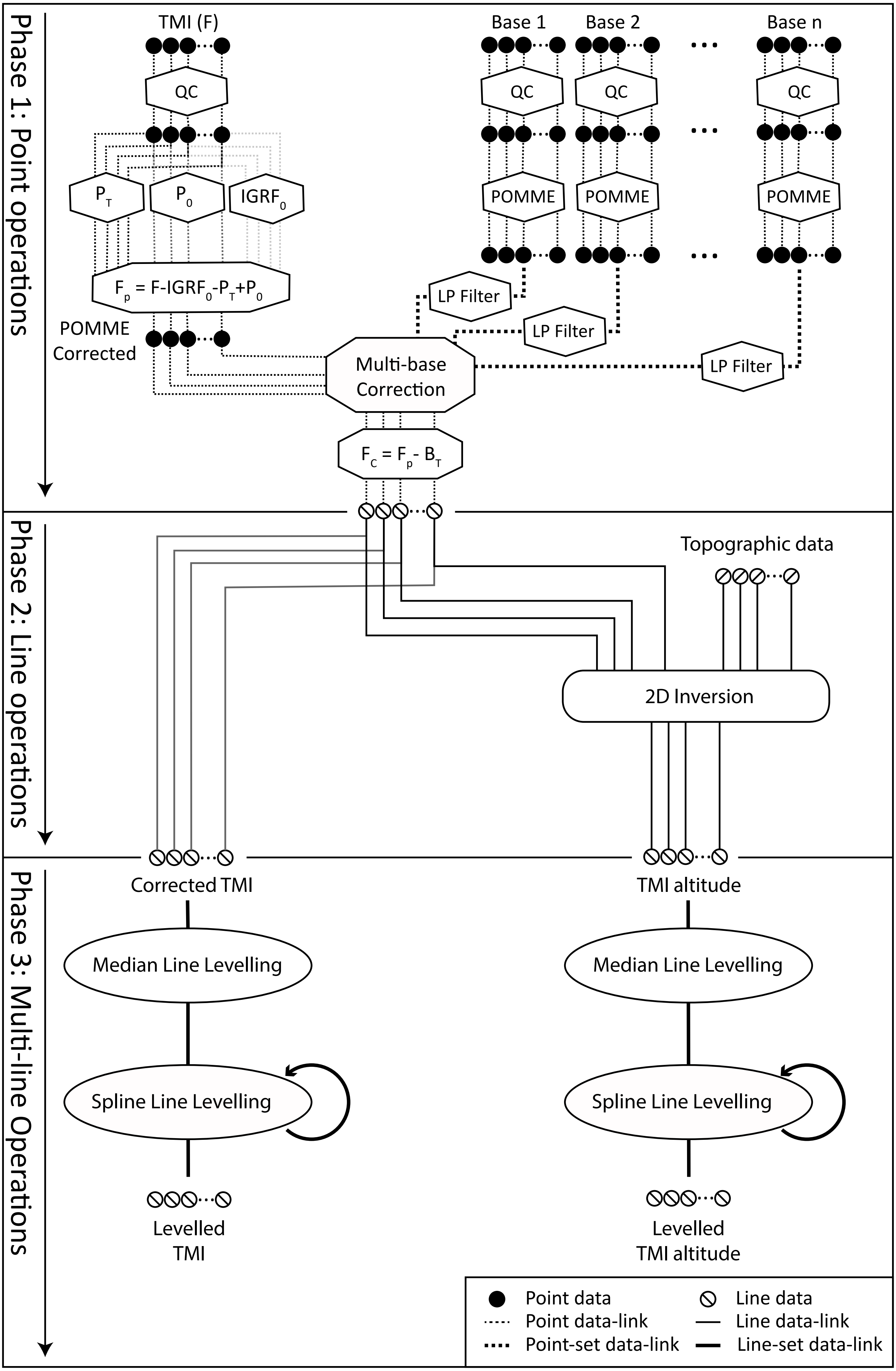
Phase 1: Point operations
TMI (F)
Base 1
Base 2
Base n
QC
QC
QC
QC
P_T
P_0
IGRF_0
POMME
POMME
POMME
F_p = F-IGRF_0-P_T+P_0
POMME Corrected
LP Filter
LP Filter
LP Filter
Multi-base Correction
F_C = F_p - B_T
Phase 2: Line operations
Topographic data
2D Inversion
Phase 3: Multi-line Operations
Corrected TMI
TMI altitude
Median Line Levelling
Median Line Levelling
Spline Line Levelling
Spline Line Levelling
Levelled TMI
Levelled TMI altitude
Point data
Point data-link
Point-set data-link
Line data
Line data-link
Line-set data-link

Figure 3.

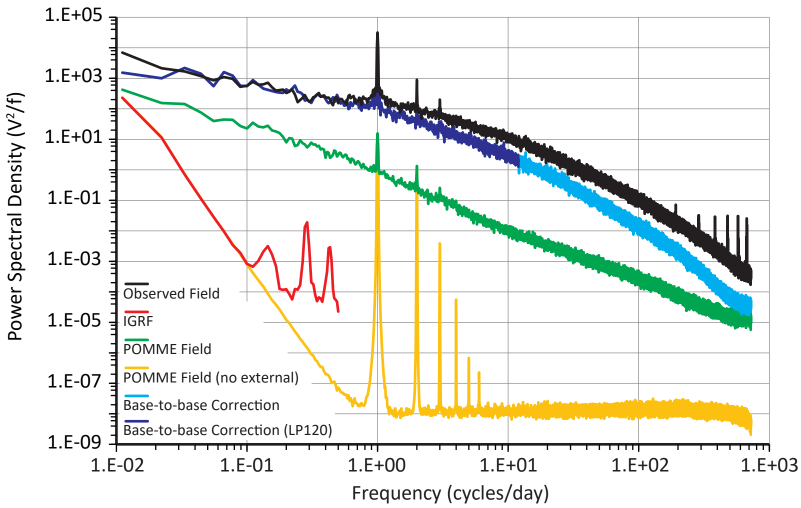
1.E+05
1.E+03
1.E+01
1.E-01
1.E-03
1.E-05
1.E-07
1.E-09
Power Spectral Density (V²/f)
Observed Field
IGRF
POMME Field
POMME Field (no external)
Base-to-base Correction
Base-to-base Correction (LP120)
1.E-02
1.E-01
1.E+00
1.E+01
1.E+02
1.E+03
Frequency (cycles/day)

Figure 4.

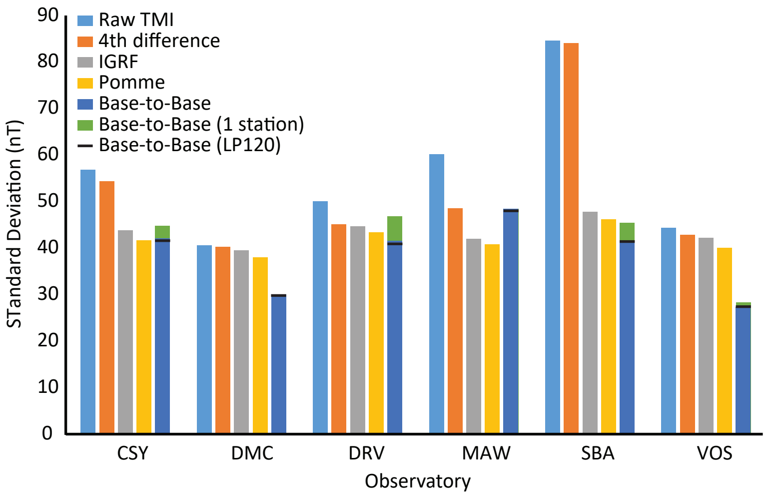

90
80
70
60
50
40
30
20
10
0
Raw TMI
4th difference
IGRF
Pomme
Base-to-Base
Base-to-Base (1 station)
Base-to-Base (LP120)
STandard Deviation (nT)
CSY
DMC
DRV
MAW
SBA
VOS
Observatory

Figure 5.

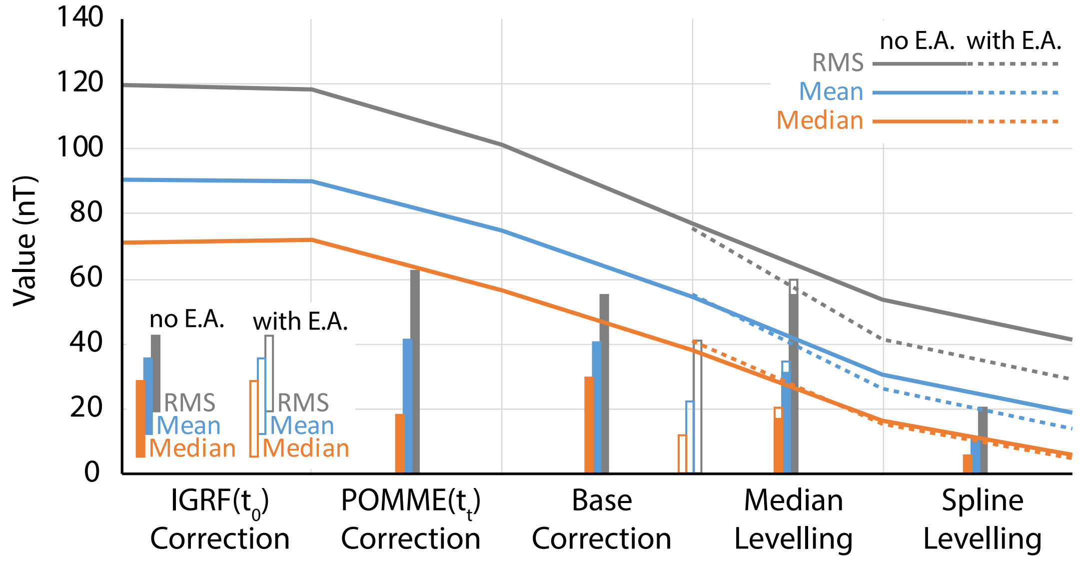

Value (nT)
140
120
100
80
60
40
20
0
no E.A. with E.A.
RMS
Mean
Median
no E.A.
with E.A.
RMS
Mean
Median
RMS
Mean
Median
IGRF(t0) Correction
POMME(tt) Correction
Base Correction
Median Levelling
Spline Levelling

Figure 6.

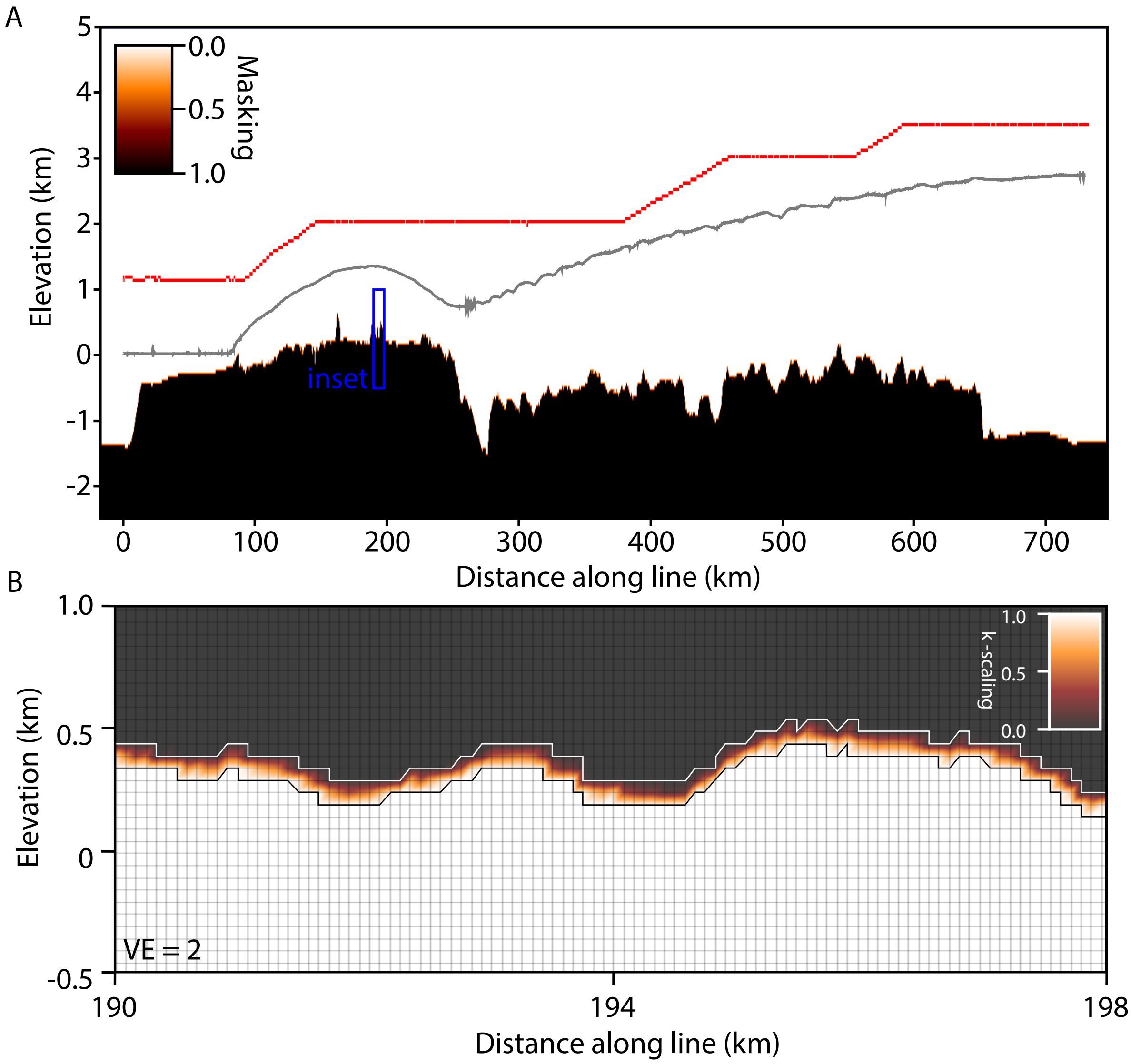

A
Masking
0.0
0.5
1.0
Elevation (km)
5
4
3
2
1
0
-1
-2
inset
0
100
200
300
400
500
600
700
Distance along line (km)
B
1.0
0.5
0
-0.5
Elevation (km)
k-scaling
1.0
0.5
0.0
VE = 2
190
194
198
Distance along line (km)

Figure 7.

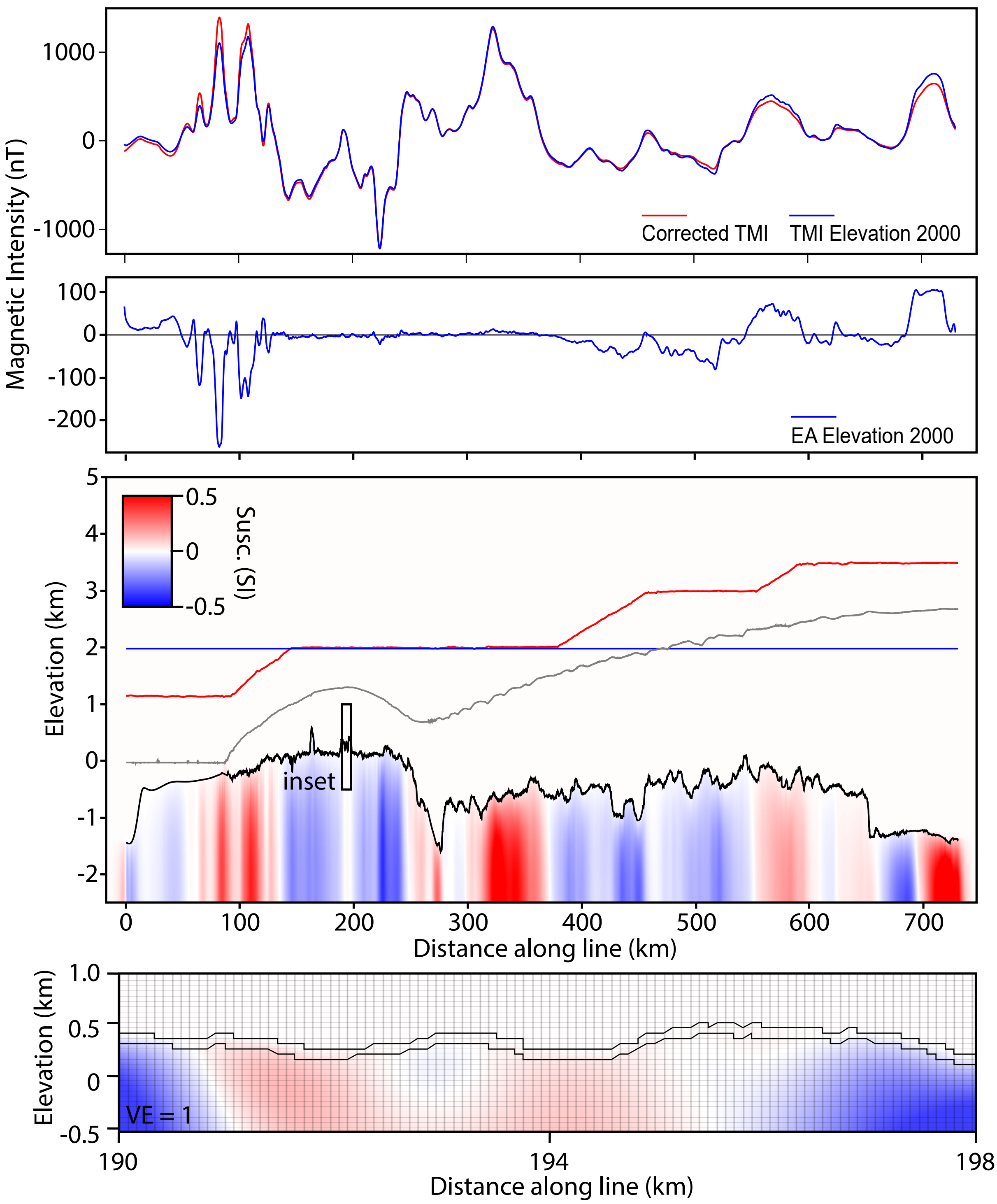

Magnetic Intensity (nT)
1000
0
-1000
Corrected TMI
TMI Elevation 2000
100
0
-100
-200
EA Elevation 2000
Elevation (km)
5
4
3
2
1
0
-1
-2
0.5
0
-0.5
Susc. (SI)
inset
0
100
200
300
400
500
600
700
Distance along line (km)
Elevation (km)
1.0
0.5
0
-0.5
VE = 1
190
194
198
Distance along line (km)

Figure 8.

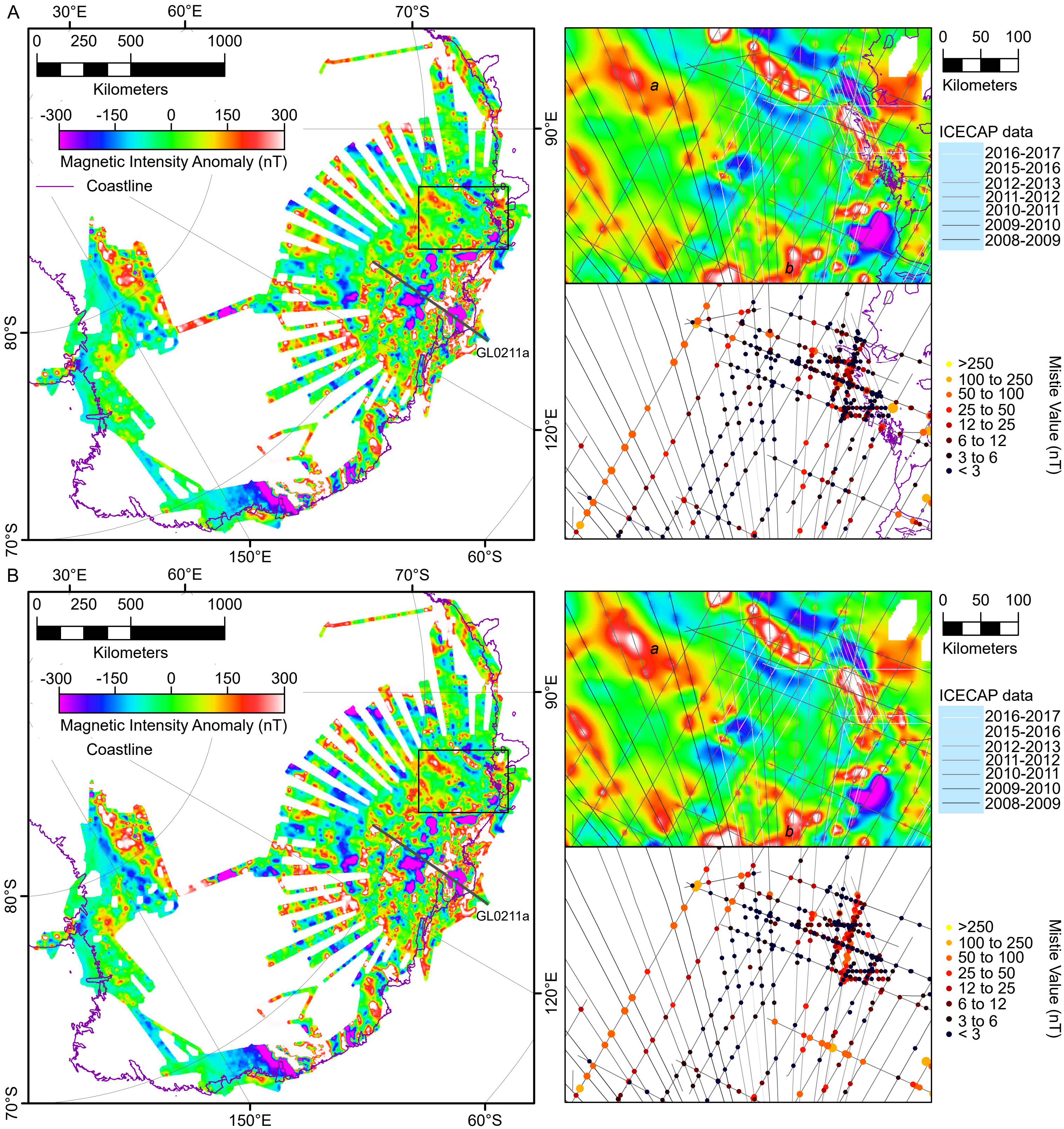
A
30°E
60°E
70°S
0
250
500
1000
Kilometers
-300
-150
0
150
300
Magnetic Intensity Anomaly (nT)
Coastline
90°E
80°S
GL0211a
120°E
70°S
150°E
60°S
0
50
100
Kilometers
a
b
ICECAP data
2016-2017
2015-2016
2012-2013
2011-2012
2010-2011
2009-2010
2008-2009
>250
100 to 250
50 to 100
25 to 50
12 to 25
6 to 12
3 to 6
< 3
Mistie Value (nT)
B
30°E
60°E
70°S
0
250
500
1000
Kilometers
-300
-150
0
150
300
Magnetic Intensity Anomaly (nT)
Coastline
90°E
80°S
GL0211a
120°E
70°S
150°E
60°S
0
50
100
Kilometers
a
b
ICECAP data
2016-2017
2015-2016
2012-2013
2011-2012
2010-2011
2009-2010
2008-2009
>250
100 to 250
50 to 100
25 to 50
12 to 25
6 to 12
3 to 6
< 3
Mistie Value (nT)